THE ASTROPHYSICAL JOURNAL, 406:470–476, 1993 April 1

HETEROGENOUS ARRAY OBSERVATIONS OF IC 342: THE CO ISOTOPIC RATIO

M. C. H. WRIGHT,[1] S. ISHIZUKI,[2] J. L. TURNER,[3] P. T. P. HO,[4] AND K. Y. LO[5]

Received 1992 July 13; accepted 1992 September 25

ABSTRACT

We present images of the ^{13}CO and ^{12}CO $J = 1–0$ emission from the nuclear region of the galaxy IC 342 with 3″ resolution. The images were obtained by combining data from the BIMA, OVRO, and Nobeyama millimeter arrays. The data processing using the MIRIAD software is described in some detail. The ^{12}CO and ^{13}CO images are very similar in appearance with an average $^{12}CO/^{13}CO$ ratio of ~ 9 over the central arcminute. The molecular gas forms two spiral features with a number of prominent peaks which are also seen in HCN emission. The $^{12}CO/^{13}CO$ line ratio varies from 3 to 24 with peaks at the position of the thermal continuum where the gas is heated by the star formation, and further out in the spiral features where the gas density is reduced. The molecular emission peaks correspond to molecular clouds with diameters 20–50 pc and masses $\sim 10^6\ M_\odot$. The total molecular mass within the central arcminute is $4.4 \times 10^7\ M_\odot$. The CO emission peaks lie between the more diffuse ^{12}CO emission and the peak Hα emission. This can be understood as due to compression of the gas by a density wave with the CO peaks tracing the dense cloud cores.

Subject headings: galaxies: individual (IC 342) — galaxies: ISM — galaxies: kinematics and dynamics — ISM: molecules

1. INTRODUCTION

IC 342 is a nearby, face-on Scd galaxy with strong CO emission from the nuclear region (Morris & Lo 1978; Young & Scoville 1982; Lo et al. 1984). Strong infrared (Becklin et al. 1980) and radio continuum emission (Turner & Ho 1983) suggest a population of young stars and a recent burst of star formation. The strong CO emission and low inclination ($i = 25°$) enable a detailed study of the geometry and conditions in the molecular gas in the nuclear region. At a distance of 1.8 Mpc (McCall 1989), 1″ = 8.7 pc, IC 342 is similar in size and luminosity to the Galaxy. Previous interferometric observations in ^{12}CO $J = 1–0$ emission (Lo et al. 1984; Ishizuki et al. 1990) show a barlike distribution with a transverse velocity gradient which was interpreted as due to an oval gravitational potential in the nucleus of IC 342 which could lead to enhanced star formation. Turner & Hurt (1992, hereafter TH92) interpret the velocity distribution in ^{13}CO emission as the gaseous response to a spiral density wave which extends into the nuclear region.

These extragalactic studies are often made under the assumption that molecular clouds in galaxies are uniform in their properties and resemble average Galactic clouds. This assumption is implicit in the use of the $N(H_2)/I(CO)$ conversion factor, for example, or the use of ^{13}CO to trace density. However, this may not be the case, especially in the nuclear regions of galaxies. Detailed study of gas in nearby galaxies where the spatial resolution is relatively high can address the question of the uniformity of molecular cloud properties and, in particular, the variation in cloud properties with galactic location. Comparison of CO $J = 1–0$ and $J = 2–1$ observations obtained with 14″–21″ resolution with the IRAM 30 m telescope (Eckart et al. 1990) shows spatial variations in the physical conditions of the molecular gas. The CO emission in the central kpc comes from gas with kinetic temperature ~ 30 K and H_2 density $\sim 3 \times 10^3\ cm^{-3}$.

In this paper we present images of ^{12}CO and ^{13}CO $J = 1–0$ emission at 2″–5″ resolution. Comparison of these transitions with identical beam sizes and well-sampled UV data allows us to study the variation in optical depth and temperature in the molecular gas of IC 342 with sufficient resolution to study individual molecular clouds. The ^{12}CO image is a mosaic of three fields separated by half-beam spacings obtained with the Nobeyama millimeter array. The ^{13}CO image was obtained by combining data from the BIMA[6] and OVRO millimeter arrays. Since the arrays have different primary beams and UV data sampling, the data are complementary, and combining the UV data results in a better image than can be obtained with a single instrument. The concept is similar to the heterogenous array of 4 and 10 m antennas originally proposed for the NRAO millimeter array, where arrays with different primary beams provide complementary data. In this case the data were obtained in different locations, and there are no cross-correlations between antennae of different sizes. This simplifies the data analysis, and we present the steps in making images from heterogenous array data in some detail.

2. OBSERVATIONS AND DATA REDUCTION

Observations of the ^{13}CO emission were obtained with the BIMA and OVRO three-antenna arrays. The BIMA data were obtained in five configurations of the 6.1 m antennas in 1989 January–April. The antenna gains were calibrated using observations of the quasar 3C 84 at intervals of 40 minutes. The flux scale was calibrated from observations of Mars and Venus for each configuration. The OVRO observations with three 10.4 m antennas are described by TH92. The ^{12}CO data were obtained with the five antenna Nobeyama millimeter array in

[1] Radio Astronomy Laboratory, University of California, Berkeley, CA 94720.
[2] Nobeyama Radio Observatory, Minamimaki, Minamisaku, Nagano 384-13, Japan.
[3] Department of Astronomy, UCLA, Los Angeles, CA 90024.
[4] Harvard-Smithsonian Center for Astrophysics, Cambridge, MA 02138.
[5] Department of Astronomy, University of Illinois, Urbana, IL 61801.

[6] The Berkeley Illinois Maryland Array is operated with support from the NSF.

three fields spaced by 30″ in declination during 1988 December to 1989 April. The data cover spatial frequencies from λ6600 to λ100980 with a 70″ primary beamwidth. We used 3C 84 as both gain and flux calibrator. We calibrated 3C 84 versus Mars and Uranus and adopted a constant flux density of 14.7 Jy.

The data were analyzed with the MIRIAD software (Wright & Sault 1991). The entire reduction procedure was controlled by a shell script which passes control to a series of MIRIAD tasks. The script was also used to combine data for the galaxy M51 obtained in several fields with the BIMA array and the Onsala 20 m antenna (Adler et al. 1992). The script is easily modified to handle situations where heterogenous data sets are used to produce a mosaic of images of multichannel data. The calibration and imaging of the data are controlled by a number of parameters, such as the primary beam size and the flux density scale. It is relatively easy to build expertise into the script to check the effect of these parameters, while keeping the individual MIRIAD tasks simple and easy to maintain. The script is written in UNIX C shell and was run on both a Sun workstation and the CRAY computer at the University of Illinois.

The basic philosophy of the data reduction is to make the simplest image which is consistent with all the data as well as the known system parameters and errors. The aim is to produce well-calibrated images which can be used for quantitative comparison to determine the $^{12}CO/^{13}CO$ line ratio. In concept the processing is very similar to the maximum entropy algorithm described by Cornwell (1988). The process described here allows more control of the calibration and uses the CLEAN algorithm to deconvolve the instrumental response.

The steps used to combine the data are as follows:

1. Make a low-resolution map for the whole field of interest.
2. Generate a model for the large-scale source structure from this map.
3. Extract fields corresponding to pointing centers for each instrument.
4. Compare the data for each instrument using a common UV coverage.
5. Combine the UV data from each instrument for each pointing center.
6. Make a mosaic of the data from each pointing center to obtain a new image.

2.1. *Combination of ^{13}CO data from BIMA and OVRO Arrays*

For the ^{13}CO data we combined the UV data from the BIMA array in a 130″ field of view, and from the OVRO array in a 70″ field of view offset from the BIMA pointing center by 2″. We first made a low-resolution map from the BIMA UV data which are well sampled for spatial frequencies down to the dish diameter. For IC 342 the structures observed in each velocity channel are smaller than 30″ and are well represented in this image. Since the synthesized beam was very clean, we used this image directly as the low-resolution model in step 2. In general we would generate a model by deconvolving the low-resolution image. For larger sources a better model is obtained from data which contain even shorter UV spacings, obtained for example from a single dish image as was the case for M51. (Adler et al. 1992.)

In step 3 we taper the model by the primary beam for the OVRO antenna. The effective primary beam might be broadened by random pointing errors or focus errors. The primary beam is therefore an adjustable parameter in the process, and we tried using Gaussian beam profiles with FWHM from 35″ to 120″.

In step 4 we check the consistency and calibration of the BIMA and OVRO data by making separate multichannel images from BIMA data weighted by the OVRO primary beam response, and from the OVRO data with the same UV coverage, primary beam, and velocity intervals. These images were compared to establish a consistent calibration. Errors in the flux scale, primary beam, and passband calibration are readily apparent. The two data sets were found to be consistent with the a priori calibration and a primary beam size of 60″–70″. In the script we tried to derive the relative calibration by dividing the UV data for both pointing centers by the model. The resulting visibility data can be Fourier inverted to give the observed point-spread function for each channel (corrupted by errors in the data and in the model). The amplitude of the point-spread function can, in principle, be used to adjust the relative calibration of the data. For these data, the noise, rather than systematic effects, limits the relative calibration accuracy to about 20%. The measured flux densities of the ~20 brightest quasars used for flux calibration at OVRO, BIMA, and Nobeyama observatories agree within about 10%.

We then combined the BIMA and OVRO UV data. The relative weight of each data set determines the shape and size of the synthesized beam. We made two series of images. With the data weighted to obtain the best S/N the synthesized beam size was 5.″7 × 4.″7; with uniform weighting the beam was 3.″0 × 2.″6.

2.2. *Mosaic of ^{12}CO Data from the Nobeyama Array*

For the ^{12}CO data we made a mosaic of the cleaned images by weighting the data for each pointing center by the primary beam response. The procedure can now be iterated by using this image as the initial model. The common model, which contains structure from all pointing centers, is tapered for each pointing center and used as the starting point in subsequent deconvolution. By incorporating information from the adjacent pointings, deconvolution of the extended structures should be more reliable. The final model was convolved by a 4.″3 × 2.″5 beam corresponding to the synthesized beamwidth for natural weighting of the central field data. We also made an image with 2.″1 × 1.″6 using uniform weighting for the central field observations to investigate the effect of beam averaging, and to estimate the peak brightness temperature.

3. RESULTS

Figure 1 shows the ^{13}CO images obtained from the combined BIMA and OVRO data at a 5.5 km s^{-1} resolution. We used the same velocity intervals as TH92, and this figure may be directly compared with their Figure 3. Additional large-scale structure sampled by the BIMA array can be seen in our Figure 1. This is especially striking at velocities near 20 km s^{-1}. The image is also cleaner in appearance. Isolated peaks in the original OVRO map probably result from difficulties in deconvolving the poorly sampled large-scale structure. The rms noise is 20 mJy in a 5.″7 × 4.″7 beam (0.07 K). The isovelocity map derived from the combined UV data is very similar to Figure 4 of TH92, and the addition of the large-scale structure does not affect the detailed shape of the velocity perturbations which TH92 interpret as due to a spiral density wave.

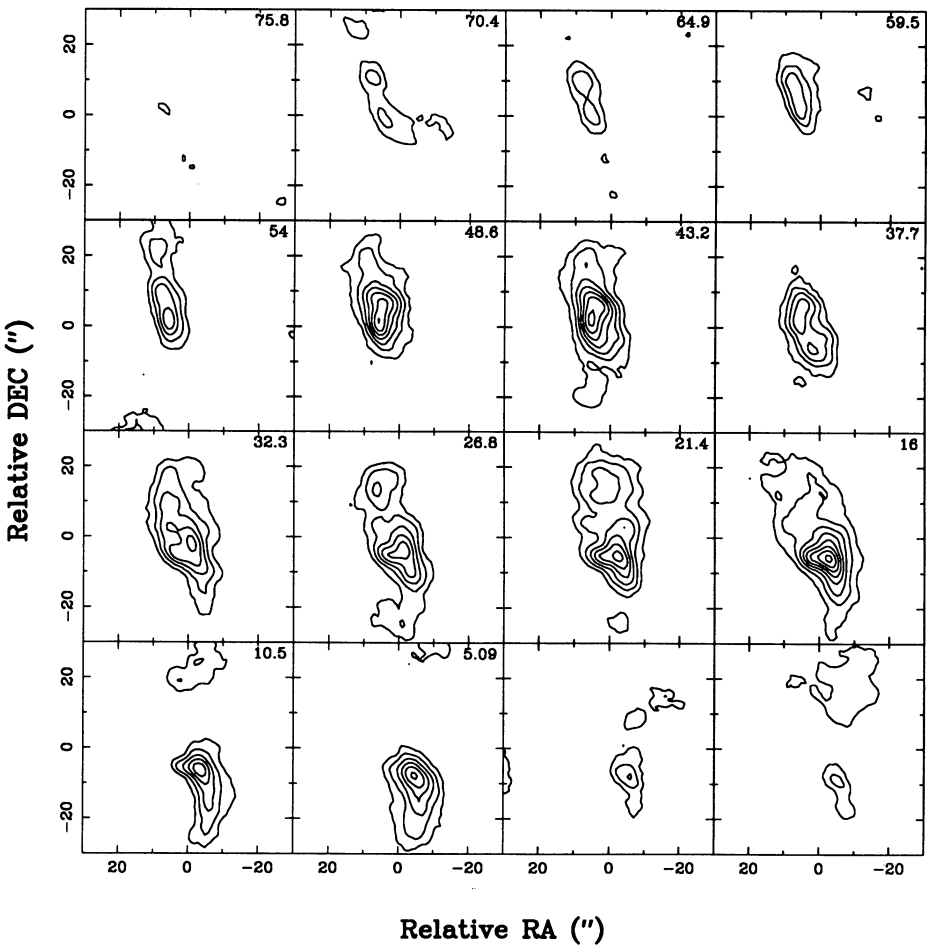

FIG. 1.—^{13}CO images obtained from the combined BIMA and OVRO data. Contour interval 60 mJy beam^{-1} (0.22 K in a 5".7 × 4".7 beam). Center position: R.A. (1950) = 03^{h}41^{m}57^s.0, decl. (1950) = 67°56'30".0.

Figure 2*a* shows the integrated ^{13}CO emission obtained with uniform weighting of the combined data at 5 MHz (13.6 km s^{-1}) resolution. The integrated emission includes emission in the range −67 to 137 km s^{-1} from both data sets, but omits pixel values smaller than 1.2 σ (18 mJy beam^{-1}) in the 5 MHz channels. This improves the S/N of the image of the integrated emission, but may omit any low-level emission with a high-velocity dispersion.

The integrated ^{13}CO emission from the combined data is 213 Jy km s^{-1}, about 20% larger than with the OVRO data alone, and consistent with single dish estimates. More significantly, the distribution is more extended as the BIMA data more completely sample the large-scale structure. In the original integrated intensity map (TH92, Fig. 1), the CLEAN algorithm has compensated for the missing large-scale structure by partially offsetting the zero level, but fails to determine the shape and full extent of the missing large-scale structure.

Figure 2*b* shows the integrated ^{12}CO emission obtained from a mosaic of the Nobeyama data. The synthesized beam is 4".3 × 2".5 somewhat different in shape from the beam obtained for the combined ^{13}CO data. We tried using each convolving beam on both integrated intensity maps. The differences are not significant, and so we used the separate best fits to the synthesized beams for the ^{13}CO and ^{12}CO images. The integrated emission in Figure 2*b* is 1767 Jy km s^{-1}, in good agreement with the value reported by Ishizuki et al. (1990) for the central field. Figure 2 should be a more reliable estimate of the integrated emission as it contains data from mutiple pointing centers and does not depend so heavily on the primary beam correction for the central field. The integrated emission agrees within the 20% calibration errors with single dish measurements (Rickard & Palmer 1981; Eckhart et al. 1990). Both images in Figure 2 are corrected for the primary beam response with a function which avoids overcorrecting pixels with low S/N.

4. DISCUSSION

4.1. *Spatial Distribution of* CO *Emission*

Both ^{12}CO and ^{13}CO emission follow two spiral features with the same overall extent. The bifurcation of both arms at the edge of the field appears in both ^{12}CO and ^{13}CO emission. There are, however, detailed differences which can be seen in the ^{12}CO/^{13}CO ratio. To make an image of the ^{12}CO/^{13}CO ratio, we convolved the ^{12}CO and ^{13}CO integrated emission to a common beam size of 4" (Fig. 3). The ^{12}CO/^{13}CO ratio peaks close to the nucleus, and also further out along the spiral features. The peak close to the center can be understood as due to heating of the molecular gas by the nuclear star formation, if it is assumed that the ^{12}CO emission is optically thick and the ^{13}CO is optically thin. In that case, ^{12}CO will reflect the higher

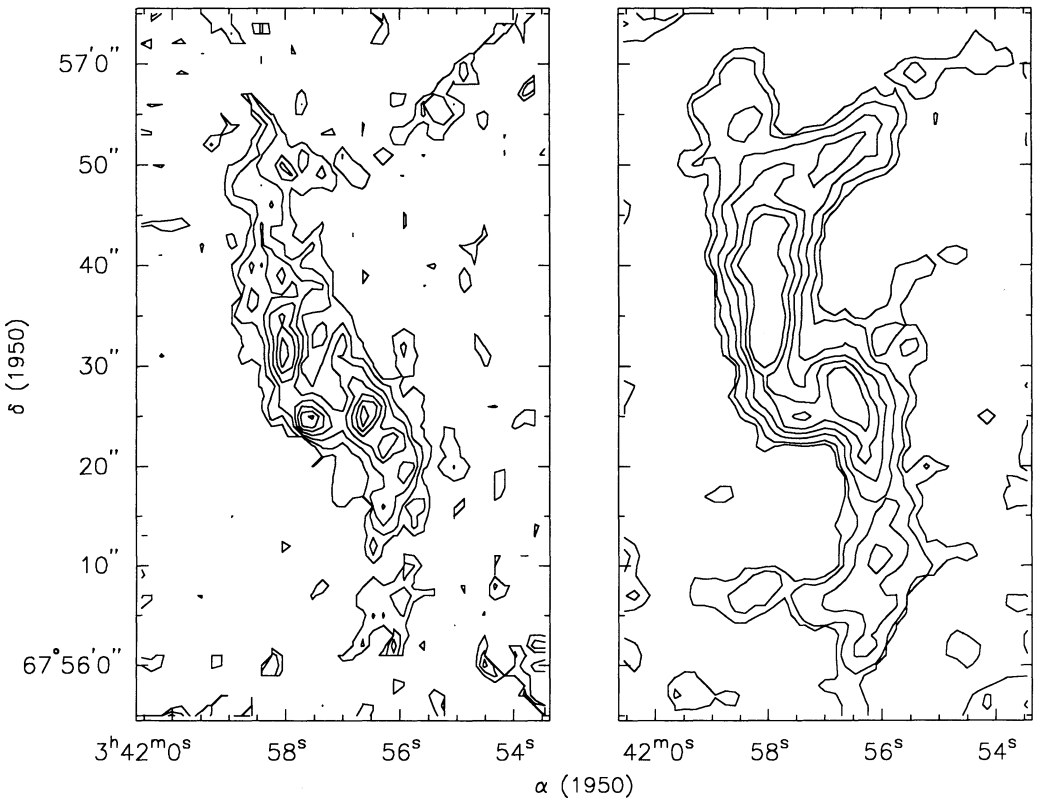

FIG. 2.—(*a*) Integrated ^{13}CO emission. Contour interval 1 Jy beam^{-1} km s^{-1} (12.7 K km^{-1} s^{-1} in a 3".0 × 2".7 beam). (*b*) Integrated ^{12}CO emission. Contours 5, 10, 20, 30, and 40 Jy beam^{-1} km s^{-1} (8.5 K Jy^{-1} in a 4".3 × 2".5 beam).

gas temperature, while ^{13}CO will reflect the level population which will actually decrease with increasing temperature. This is consistent with the peak in the $^{12}CO/^{13}CO$ ratio being driven by both a maximum in the ^{12}CO and a minimum in the ^{13}CO at the position of the thermal radio continuum (Turner & Ho 1983). Further out on the spiral arms, both north and south, the $^{12}CO/^{13}CO$ ratio peaks again. This time, however, the ratio is accompanied by a decrease in both ^{12}CO and ^{13}CO. This indicates that the CO emission is becoming more optically thin, reflecting a decrease in column density away from the nucleus. The ratio is significantly higher in the NW arm. The ratio of the integrated emission within the images is 9 ± 1. Single dish estimates of 9–15 (Rickard & Blitz 1985; Young & Sanders 1986) will vary according amount of extended emission in the field mapped.

4.2. *Comparison with Other Emission*

Figure 3 also shows contours of the 6 cm emission (Turner & Ho 1983). The 6 cm emission traces both thermal and non-thermal emission rather than dust emission. In this image we have reprocessed the 6 cm continuum data to trace the low brightness emission. The $^{12}CO/^{13}CO$ ratio increases as the 6 cm emission runs out, consistent with the decreasing gas density along the spiral features. The maximum in the $^{12}CO/^{13}CO$ ratio along the spiral features is displaced to the trailing side of the CO peaks. Thus, the peak ^{13}CO emission lies between the bulk of the ^{12}CO emission and the peak Hα emission (see TH92, Fig. 2.) If the ^{13}CO preferentially traces dense cloud cores, and the ^{12}CO emission traces less dense gas (Downes et al. 1992), then this can be understood as due to compression of the gas by a density wave.

4.3. *Velocity Dispersion*

The velocity dispersion was derived from the second moment of the 5.5 km s^{-1} resolution maps above a 40 mJy threshold. The rms velocity dispersion is 12–15 km s^{-1} over most of the galaxy, rising to 25 km s^{-1} due to inadequate resolution of the velocity gradient to the NE and SE. The line profiles are consistent with the velocity dispersion derived from the second moment, except in the north of the galaxy where the two ears are separated in velocity by 20 km s^{-1}, and the line profile is clearly a blend of two features.

4.4. *Molecular Clouds*

Figure 4 shows the ^{12}CO and ^{13}CO spectra at the positions of the inner peaks designated A–E in HCN emission (Downes et al. 1992). The $^{12}CO/^{13}CO$ ratio for the clouds was estimated by convolving the ^{12}CO and ^{13}CO images to a common beam size of 4".4 and fitting a single Gaussian at the position of the ^{12}CO peak. Table 1 summarizes the fits for the inner five peaks in ^{12}CO, ^{13}CO, and HCN (Downes et al. 1992). The peak positions measured in the three molecular lines agree within the errors (~1" for well-defined peaks), except for peak B which coincides better with the thermal continuum and 2 μm emission in HCN and ^{12}CO emission, consistent with the gas being heated by the star formation process. The velocities are in good agreement except for peak B where HCN seems to be redshifted with regard to the ^{12}CO and ^{13}CO emission,

perhaps indicating an interaction between the star formation and the dense molecular gas, such as a molecular outflow.

The HCN line widths are significantly larger than those measured from the ^{12}CO and ^{13}CO spectra if we exclude spectra which are clearly spectral blends. The line widths are not significantly higher when measured at 5″ resolution, so the larger HCN line widths are not caused by broadening due to the measured velocity gradient ($\sim$10–15 km s^{-1} in a 5″ beam [43 pc at distance 1.8 Mpc]). The higher line width might be understood if the HCN is enhanced by shocks, possibly from a spiral density wave. In this case the HCN abundance might be enhanced by a factor of up to 10^5 (Mitchell & Deveau 1983), and the cloud masses deduced from HCN may not be reliable.

4.5. *Opacity of* CO *Emission*

Comparison of the line ratios of the $J = 3$–2, $J = 2$–1, and $J = 1$–0 transitions for both ^{12}CO and ^{13}CO (Eckart et al. 1990; Ho et al. 1990; Wall & Jaffe 1990; Irwin & Avery 1992) suggest that the CO emission is from warm gas with moderate opacity. A possible interpretation is that the observed brightness temperatures are measures of the different beam filling factor for ^{12}CO and ^{13}CO. If we assume an excitation temperature of 42 K equal to the dust temperature (Becklin et al. 1980), and that the ^{13}CO is close to optically thick, we estimate beam filling factors of $\sim$15% for ^{12}CO and $\sim$5% for ^{13}CO consistent with the suggestion (Downes et al. 1992) that the ^{13}CO emission comes mainly from the cloud cores. The peak brightness temperature measured on the 2.″1 × 1.″6 resolution image is 28 ± 5 K in cloud C, in good agreement with the gas kinetic temperature estimated by Ekhart et al. (1990). Another interpretation of the CO line ratios is that the observed brightness temperatures reflect temperature variation within the clouds. The optically thinner ^{13}CO probes the lower temperatures within the cloud cores that are protected from UV dust heating.

4.6. *Mass Estimates and Stability of Molecular Clouds*

Eckhart et al. (1990) estimate that a $N(H_2)/I(CO)$ conversion factor of 3–4 10^{20} is appropriate for the molecular gas in IC

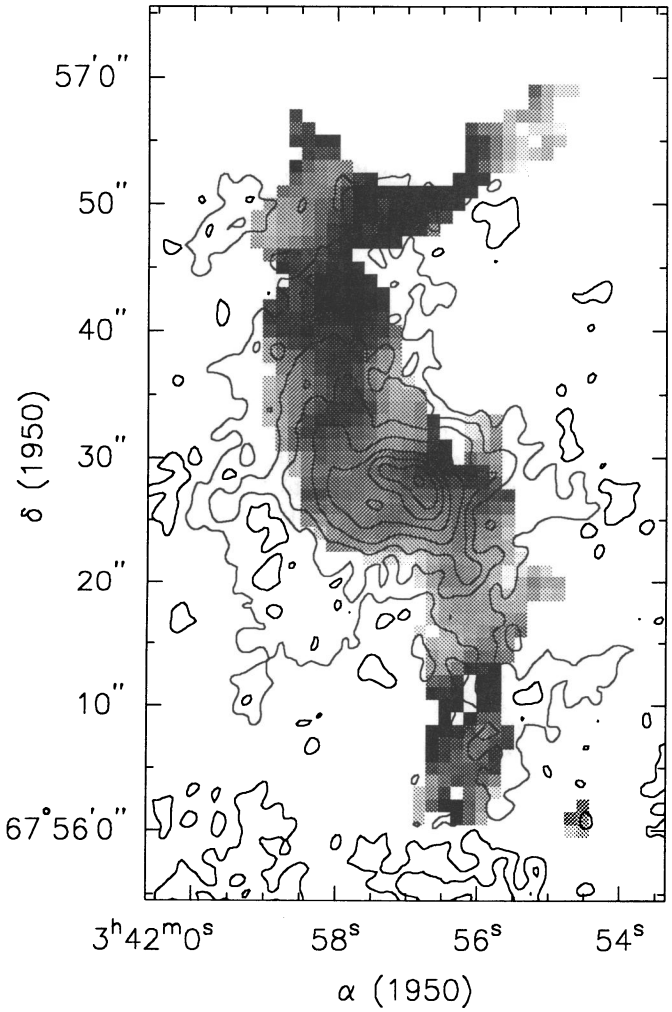

FIG. 3.—^{12}CO/^{13}CO ratio gray scale (0 = white, 24 = black), overlaid on 6 cm continuum emission contours (0.05, 1.25, 2.5, 5, 1, 1.5, 2, 2.5 mJy beam^{-1} in a 2″ × 1.″7 beam).

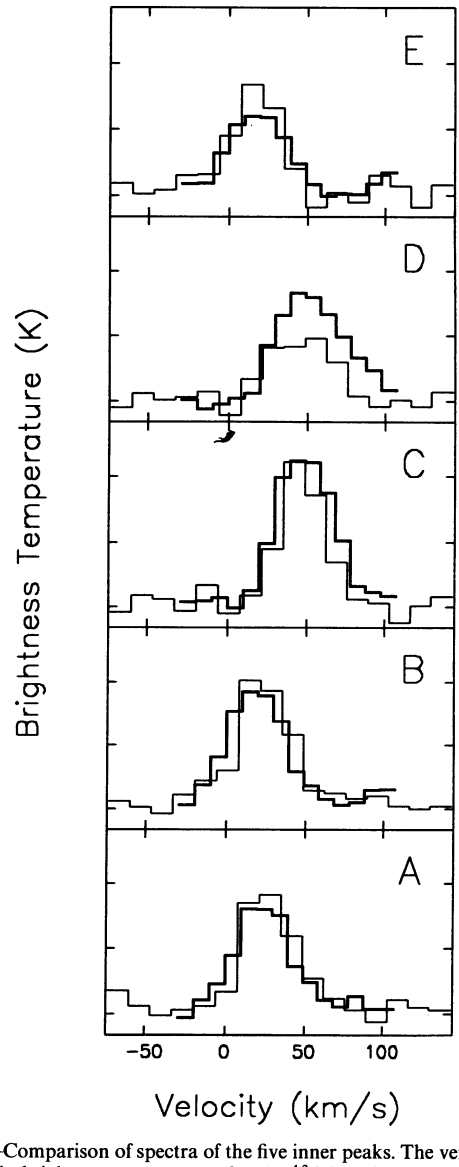

FIG. 4.—Comparison of spectra of the five inner peaks. The vertical scale is −1 to 9 K in brightness temperature for the ^{12}CO emission (*thick lines*), and −0.2 to 1.8 K for the ^{13}CO emission (*thin lines*). All spectra have been convolved to 4.″4 resolution.

TABLE 1

IC 342 MOLECULAR CLOUD PARAMETERS

PARAMETER	CLOUD A	B	C	D	E
Positions (R.A., Decl.)[a]					
HCN[b]	(2".5, −5".5)	(−1".5, −2".6)	(5".8, 1".8)	(4".5, 7".8)	(−3".2, −5".6)
^{12}CO	(2.5, −4.9)	(−2.1, −3.4)	(5.8, 3.1)	(6.1, 10.9)	(−4.4, −9.7)
^{13}CO	(3.3, −5.3)	(−2.0, −5.1)	(5.8, 1.6)	(6.5, 9.7)	(−4.2, −7.7)
Peak T_a (K)					
^{12}CO	5.2	6.0	7.6	5.2	4.0
^{13}CO	1.0	1.3	1.6	0.7	1.0
Line Ratio					
^{12}CO/^{13}CO	5.2	4.6	4.8	7.4	4.0
Velocities (km s^{-1})					
HCN	27 ± 5	30 ± 5	48 ± 5	49 ± 5	17 ± 5
^{12}CO	23 ± 2	19 ± 2	48 ± 2	51 ± 2	17 ± 2
^{13}CO	24 ± 2	22 ± 2	46 ± 2	46 ± 4	17 ± 2
Width FWHM (km s^{-1})					
HCN	58 ± 5	41 ± 5	56 ± 5	60 ± 5	48 ± 5
^{12}CO	37 ± 2	39 ± 2	41 ± 2	47 ± 3	40 ± 4
^{13}CO	38 ± 4	39 ± 4	34 ± 4	42 ± 7	33 ± 3

[a] (R.A., Decl.) positions are relative to R.A. = 03^{h}41^{m}57^s.0, Decl. = 67°56'30".

[b] The estimates for HCN are taken from Downes et al. 1992.

342. Consistent estimates are obtained using a factor 4×10^{21} for masses determined from ^{13}CO-integrated emission (cf. Young & Scoville 1982). Using these conversion factors, the molecular hydrogen mass within the images is $3.4 \times 10^7\ M_\odot$. The individual clouds have sizes 3"–5" (20–50 pc). Assuming a spherical geometry we obtain average densities of $3–7 \times 10^3$ cm^{-3} and masses $\sim 10^6\ M_\odot$ for the cloud cores. The measured velocity dispersion is 7–21 km s^{-1}, some of which may be attributed to the velocity gradient within the beam, although the velocity dispersion measured from the 2".1 × 1".6 ^{12}CO image is not significantly reduced. The virial mass estimated from the measured size and velocity dispersion is $0.4–1.6 \times 10^6$ $M_\odot$, thus the cloud cores are about in virial equilibrium, but are still subject to tidal disruption and may break up and spiral into the nucleus, similar to the predicted fate of molecular clouds in the Galactic center (Stark et al. 1991).

The five inner clouds have similar sizes, brightness, and line widths in ^{12}CO, ^{13}CO, HCN, and NH3 (Ho et al. 1990), yet only cloud B is close to the star formation region. Clearly some other factor is necessary for triggering star formation, and the molecular peaks are not good tracers of star formation. The 2 μm peak in IC 342 is close to the dynamical center, which is close to the brightest H II region in many spiral galaxies. It appears that dynamical factors may lead to star formation, and molecular line peaks or ratios are not good tracers.

4.7. *Self-gravitating Spiral Density Wave*

The total molecular mass within a 250 pc radius, including He, is $\sim 4.4 \times 10^7\ M_\odot$ while the total mass estimated from the rotation curve is $4 \times 10^8\ M_\odot$. The molecular mass is 11% of the total, with an even higher fraction of molecular mass at smaller radii (JH92). Given these high gaseous mass fractions, the molecular spiral may be self-gravitating. The average surface density of molecular gas within 250 pc, $\Sigma \sim 700\ M_\odot$ pc^{-2}. From the rotation curve at 150 pc (JH92) we estimate the epicyclic frequency $K = 900$ km s^{-1} kpc^{-1}.

The scale length for instabilities in sinosoidal density perturbations is given by Toomre (1964) as $\Lambda_T = 4\pi^2 G\Sigma/K^2 = 150$ pc. This is close to the observed length of the spiral features. Features smaller than this will collapse on a time scale $T = 1/K\sqrt{(\Lambda_T/\Lambda - 1)} \sim 1.1 \times 10^6$ yr. Thus the molecular clouds may have formed from instabilities on a time scale of 10^6 yr. The cloud cores are displaced from the mean position of the ^{12}CO by ~ 5". Using a rotation velocity 30 km s^{-1} (in the plane of the sky) at a radius 150 pc, the cloud cores are observed to be displaced by 1.3×10^6 yr, with the star formation as indicated by the Hα emission, a further $\sim 10^6$–10^7 yr downstream. Dissociation of molecular gas into H I may also lead to an abrupt edge to molecular gas. A high-resolution H I image is required.

The velocity dispersion in the gas stabilizes the arms against collapse. The stability parameter, $Q = K\sigma_v/(\pi G\Sigma) = 1.1–1.4$ for the measured velocity dispersion, σ_v, of 12–15 km s^{-1}, indicating that the stability is marginal (e.g., Toomre 1964; Shu 1982), and that the above scenario is plausible. The change in position angle of the spiral arm at 30" radius clearly visible in both ^{12}CO and ^{13}CO emission in the northern feature, and in the ^{12}CO image in the southern arm, may correspond to a resonance. Observations at larger radii are required to accurately trace the arms beyond this feature. The apparent arm: interarm density contrast of 20:1 is a lower limit set by the S/N. Our observations do not image emission on a scale of $\sim 1'$ between the arms, but are consistent with single dish measurements within the $\sim 20\%$ calibration errors. Combination of interferometer observations with data from a large single dish antenna might improve the limits on the contrast ratio.

5. CONCLUSIONS

We have compared the ^{12}CO and ^{13}CO emission with identical beam sizes and well-sampled UV data with sufficient resolution to study individual molecular clouds. The ^{13}CO and ^{12}CO emission give consistent images of the molecular distribution in IC 342. Thus either ^{12}CO or ^{13}CO emission provides an adequate tracer of the overall molecular distribution, at least in IC 342.

Within the central arcminute, the molecular gas forms two spiral features with a number of prominent peaks which are also seen in HCN emission. The ^{12}CO/^{13}CO line ratio varies from 3 to 24 with peaks at the position of the thermal continuum where the gas is heated by the star formation, and further out in the spiral features where the gas density is reduced. The molecular emission peaks correspond to molecular clouds with diameters 20–50 pc, masses $\sim 10^6\ M_\odot$, and ^{12}CO/^{13}CO ratio ~ 5. Since only one of these molecular clouds is associated with the active star formation region, neither molecular peaks nor line ratios provide an adequate tracer of star formation.

The molecular mass within the central 500 pc is $\sim 11\%$ of the total mass and may support a self-gravitating spiral density wave. The CO emission peaks lie between the more diffuse ^{12}CO emission and the peak Hα emission. This can be understood as due to compression of the gas by a density wave with the CO peaks tracing the dense cloud cores.

The development of the BIMA array is partially supported by NSF grant AST 91-00307. The Owens Valley Millimeter Interferometer is operated with support from Caltech and NSF grant AST 87-14405 with additional operations support from UCLA. J. L. T. acknowledges partial support by NSF grant AST 90-22996. M. C. H. W. would like to thank Frank Shu for writing an inspiring textbook.

REFERENCES

Adler, D. S., Lo, K.Y., Wright, M. C. H., Rydbeck, G., Plante, R. L., & Allen, R. J. 1992, ApJ, 392, 497
Becklin, E. E., et al. 1980, ApJ, 236, 441
Cornwell, T. J. 1988, A&A, 202, 316
Downes, D., Radford, S. J. E., Guilloteau, S., Guelin, M., Greve, A., & Morris, D. 1992, A&A, 262, 424
Eckart, A., Downes, D., Genzel, R., Harris, A., Jaffe, D. T., & Wild, W. 1990, ApJ, 348, 434
Ho, P. T. P., Martin, R. N., Turner, J. L., & Jackson, J. M. 1990, ApJ, 355, L19
Irwin, J. A., & Avery, L. W. 1992, ApJ, 388, 328
Ishizuki, S., Kawabe, R., Ishiguro, M., Okumura, S. K., Morita, K.-I., Chikada, Y., & Kasuga, T. 1990, Nature, 344, 224
Lo, K. Y., et al. 1984, ApJ, 282, L59
McCall, M. L. 1989, AJ, 97, 1341
Mitchell, G. F., & Deveau, T. J. 1983, ApJ, 266, 646
Morris, M., & Lo, K. Y. 1978, ApJ, 223, 803
Rickard, L. J., & Blitz, L. 1985, ApJ, 292, L57
Rickard, L. J., & Palmer, P. 1981, A&A, 102, L13
Shu, F. H. 1982, The Physical Universe (Mill Valley: University Science Books)
Stark, A. A., Gerhard, O. E., Binney, J., & Bally, J. 1991, MNRAS, 248, 14P
Toomre, A. 1964, ApJ, 139, 1217
Turner, J. L., & Ho, P. T. P. 1983, ApJ, 268, L79
Turner, J. L., & Hurt, R. L. 1992, ApJ, 384, 72 (TH92)
Wall, W. F., & Jaffe, D. T. 1990, ApJ, 361, L45
Wright, M. C. H., & Sault, R. J. 1991, IAU Colloq. 131, 276
Young, J. S., & Sanders, D. B. 1986, ApJ, 302, 680
Young, J. S., & Scoville, N. 1982, ApJ, 258, 467
Wall, W. F., & Jaffe, D. T. 1990, ApJ, 361, L45